THE JOURNAL OF PHYSICAL CHEMISTRY A
A JOURNAL OF THE AMERICAN CHEMICAL SOCIETY

pubs.acs.org/JPCA Article

Stability and Structure of Potentially Atmospherically Relevant Glycine Ammonium Bisulfate Clusters

Annapoorani Hariharan, Conor J. Bready, Jack G. Ajello, Samantha H. Black, George C. Shields, and Christopher J. Johnson*

Cite This: J. Phys. Chem. A 2024, 128, 4268−4278 Read Online

ABSTRACT: New particle formation (NPF) is the process by which trace atmospheric acids and bases cluster and grow into particles that ultimately impact climate. Sulfuric acid concentration drives NPF, but nitrogen-containing bases promote the formation of more stable clusters via salt bridge formation. Recent computational efforts have suggested that amino acids can enhance NPF, predicting that they can stabilize new particles via multiple protonation sites, but there has yet to be experimental validation of these predictions. We used mass spectrometry and infrared spectroscopy to study the structure and stability of cationic clusters composed of glycine, sulfuric acid, and ammonia. When collisionally activated, clusters were significantly more likely to eliminate ammonia or sulfuric acid than glycine, while quantum chemical calculations predicted lower binding free energies for ammonia but similar binding free energies for glycine and sulfuric acid. These calculations predicted several low-energy structures, so we compared experimental and computed vibrational spectra to attempt to validate the computationally predicted minimum energy structure. Unambiguous identification of the experimental structure by comparison to these calculations was made difficult by the complexity of the experimental spectra and the fact that the identity of the computed lowest-energy structure depended strongly on temperature. If their vapors are present, amino acids are likely to be enriched in new particles by displacing more weakly bound ammonia, similar to the behavior of other atmospheric amines. The carboxylic acid groups were found to preferentially interact with other carboxylic acids, suggesting incipient organic/inorganic phase separation even at these small sizes.

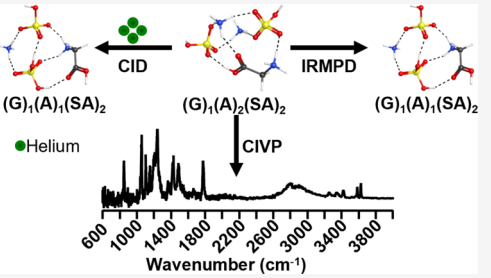

INTRODUCTION

Atmospheric aerosols have profound impacts on climate and health.[1,2] Secondary aerosols in the atmosphere start as small, gas-phase molecular clusters formed by clustering of low-volatility gases and can eventually impact climate by growing into cloud condensation nuclei (CCN).[3−5] The initial step, called new particle formation (NPF), has been suggested to account for 10−90% of CCN around the Earth.[6−10] The uncertainty in anthropogenic warming associated with aerosol-cloud interactions in climate models is large owing to a limited understanding of the various sources and sinks of particles as well as the complex nature of the NPF mechanism.[11−13] Efforts to understand NPF at a molecular level have revealed that gas phase acid−base chemistry plays a crucial role in the formation of small, thermodynamically stable "prenucleation" clusters.[14−17] As one of the most abundant trace acids in the atmosphere, sulfuric acid has been a focus of NPF research. However, bases such as ammonia, amines, and diamines have been shown to stabilize atmospherically relevant sulfuric acid clusters, thereby accelerating growth.[17−27] Proton transfer between sulfuric acid and bases leads to stabilization by a balance between Coulombic forces and hydrogen bonds in the clusters.[24]

Organic molecules have been identified as key players in both the nucleation and growth stages of new particles in the atmosphere.[28−31] Field studies have shown that particles with >1.5 nm diameter exhibit accelerated growth rates through the uptake of oxidized organic vapors. Laboratory studies have established that hydrogen bonding is important to organic molecule-sulfuric acid clusters, much like in ammonia-sulfuric acid clusters, demonstrating that organic molecules with polar functional groups (e.g., hydroxyl, carboxyl, and amino) have the potential to drive particle nucleation.[12,32,33]

Approximately 20% of fine particles detected in the atmosphere are composed of water-soluble organic nitrogen compounds (WSON).[34] Amino Acids (AAs) are a significant portion of WSON and are also a vital part of the biosphere-atmosphere nutrient cycle.[35−37] AAs are enriched in sea spray aerosols (SSAs) and are known to decrease the surface tension of CCN, thereby reducing the vapor pressure of water needed

Received: March 12, 2024
Revised: May 2, 2024
Accepted: May 6, 2024
Published: May 16, 2024

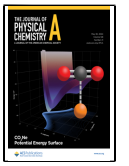

https://doi.org/10.1021/acs.jpca.4c01629
J. Phys. Chem. A 2024, 128, 4268−4278

for cloud droplet activation.[38−42] While AAs have been detected in the atmosphere over different geographic locations, with sources such as volcanic emissions, biomass burning, and emissions from marine biota, there is no clear information on the exact concentrations of free amino acids.[34,37,43−52] The amphiprotic nature of amino acids (AAs), characterized by the presence of at least two polar functional groups ($-NH_2$ and −COOH), can facilitate strong intermolecular hydrogen bonding with other atmospheric components.

Recent computational evidence has suggested that, while AAs are unlikely to cluster and grow to CCN-relevant sizes on their own, they can enhance the stability of sulfuric acid clusters.[50,53] Glycine, the simplest amino acid, has been shown to favorably interact with sulfuric acid via multiple protonation states, stabilizing it in a manner akin to ammonia.[54,55] Anionic glycine (deprotonated at the −COOH end) had the most favorable interaction with sulfuric acid, wherein both protons from sulfuric acid were shared with glycine's carboxylate group. While cationic glycine (protonated at the $-NH_2$ end) had a slightly less favorable interaction (higher formation free energy) with sulfuric acid alone, it had a more favorable interaction in the presence of ammonia, sulfuric acid, and water than deprotonated glycine.[54] Serine and alanine have been shown to have an even larger stabilizing effect on sulfuric acid than glycine, with formation free energies of alanine-sulfuric acid clusters being comparable to those of the ammonia-sulfuric acid system.[32,55] Alanine-sulfuric acid clusters are known to exhibit hydrogen bonding between sulfuric acid and the amino group of alanine as well as hydrogen bonds between water and alanine via the carboxylic acid group.[32]

To our knowledge, there have been no experimental studies probing the stability and structures of clusters composed of an amino acid, sulfuric acid, and other common atmospheric precursors to confirm these predictions. We have utilized mass spectrometry and gas-phase vibrational spectroscopy to probe the stability and structures of clusters composed of glycine (G), ammonia (A), and sulfuric acid (SA) molecules. We chose G for its relatively simple structure as well as its relatively high abundance in atmospheric aerosols. Five clusters, namely, $(G)_1(A)_1(SA)_1$, $(G)_2(A)_0(SA)_1$, $(G)_1(A)_2(SA)_2$, $(G)_2(A)_1(SA)_2$, and $(G)_3(A)_0(SA)_2$, are studied in this work, showing that protonated G plays a complex role in clusters of these types. We further highlight commonly found bonding arrangements in the clusters that hint at an organic−inorganic phase separation, which can impact the atmospheric processing of particles of this type.

METHODS

The cationic clusters discussed in this work were generated by electrospray ionization (ESI) of solutions containing 1 mM of glycine (Sigma-Aldrich, ACS reagent, ≥98.5%) and 1 mM of ammonium sulfate (Sigma-Aldrich, ACS reagent, ≥99%) in 75%/25% acetonitrile/water and 0.1% (v/v) formic acid. The ratio of glycine to the salt in the solutions was varied to control the composition of the clusters formed as discussed below.

The clusters were initially generated via ESI using a Thermo Scientific LTQ XL linear ion trap mass spectrometer. The relative stability of the clusters was characterized via collision-induced dissociation (CID) experiments. Each cluster of interest was subjected to collisions with background gas (Helium), ultimately leading to fragmentation. The m/z-dependent normalized collision energy (NCE) parameter of the LTQ XL was utilized (in increments of 2.5% starting from 0 to 10% NCE and increments of 5% between 10 and 20% NCE) to achieve the stepwise dissociation of the clusters. The activation time for each CID experiment was 30 ms. Each plotted mass spectrum is an average of 100 scans. NCE-resolved breakdown curves were generated using a home-built Python code that quantifies the absolute intensities of fragments as a function of NCE.

Vibrational spectroscopy experiments were carried out in a home-built guided ion beam/ion trap/tandem time-of-flight (ToF) photofragmentation mass spectrometer described in detail elsewhere.[26] Once generated via ESI, the ions were transported into a vacuum system and accumulated in a room temperature octopole ion trap. From here, the ions were transferred to an octopole ion trap mounted onto a closed-cycle cryocooler capable of operating between 3 and 310 K. The cryogenic ion vibrational predissociation (CIVP) spectra discussed in this work were collected as previously described.[24,27,56] Briefly, buffer gas cooling of the clusters to the temperature of the ion trap encouraged the formation of "tagged" clusters whereby a single N_2 (40−50 K) or D_2 (17−20 K) molecule physisorbed onto the clusters. The tagged clusters were then extracted into the ToF stage and ions with the mass of interest were intersected by a tunable infrared (IR) laser pulse from an Nd:YAG pumped OPO/OPA system (LaserVision). Absorption of a single photon resonant with a vibrational transition of the cluster resulted in the desorption of the tags, thereby producing fragment ions that subsequently were mass separated and quantified by a reflectron mass spectrometer. The CIVP spectra of each cluster were generated by computing the ratio of the integrated intensity of the untagged fragment ions to the sum of the integrated intensities of both the tagged parent and the untagged fragment ions, corrected for laser power, at each wavelength.

The photochemical decomposition pathways of the tag-free clusters were obtained by exposing the clusters to a high-power laser pulse at the bisulfate OH stretching frequency (3620 cm^{-1}). This intersection resulted in the absorption of multiple photons, leading to the generation of fragment ions through the ejection of specific cluster components. The number of fragments and the total yield of each fragment were monitored as a function of both laser power and reflectron voltage.

Two experiments, using a two-laser scheme, were carried out to identify specific structural isomers. For IR−IR hole burning experiments, the first laser was introduced such that the pulses intersected the ions in the cryogenic ion trap. The frequency of this laser was fixed at a transition unique to a specific isomer leading to the desorption of tags from just that isomer. The remaining tagged clusters, after a ToF separation, were probed by the second laser scanning the entire spectral region of interest much like the CIVP experiment described above. IR−IR double resonance spectra were collected by slightly modifying the above procedure.[57,58] The first laser was scanned over the IR region of interest while the second laser was kept fixed at an infrared wavelength corresponding to a vibrational transition distinct to one specific isomer. The spectrum of each isomer was then obtained by monitoring the depletion of the ion signal.

To calculate the geometries of the clusters, configuration sampling was first used to generate hundreds of thousands of possible confirmations by using the genetic algorithm-based protocol in the OGOLEM program.[59,60] A pool size of 1000 was used, and 20,000 global optimizations were allowed. The

https://doi.org/10.1021/acs.jpca.4c01629
J. Phys. Chem. A 2024, 128, 4268−4278

resulting structures were then optimized at the GFN2 semiempirical level of theory. Due to the uncertainties associated with the low-level semiempirical methods, a cutoff energy of 30 kcal mol^{-1} above the global minimum was employed to ensure the highest possible chance of finding the minimum without extraneous calculations. The GFN2 structures were reoptimized using the ωB97X-D/6-31++G** level of theory on the Gaussian 16 Rev. B01 program.[61] All electronic energies from structures within 8 kcal mol^{-1} of the DFT minimum were recalculated with the domain-based local pair natural orbital coupled cluster, or DLPNO−CCSD(T), method with single, double, and semicanonical perturbative triple excitations with three Dunning basis sets, cc-pVnZ (n = D, T, Q) using ORCA 5.0.1. Thermodynamic estimates of $H°$, $S°$, and $G°$ were computed at 40, 216.65, and 298.15 K and 1 atm using the THERMO.pl script from the National Institute of Science and Technology and the ωB97X-D frequencies, which were scaled by a factor of 0.971 to account for some anharmonicity. These were combined with the electronic energies from a 4−5 inverse polynomial complete basis set extrapolation of the three DLPNO−CCSD(T) electronic energies to get the final Gibbs free energies.[62,63] For a more detailed explanation of the computational methodologies, the reader is referred to the recent review by Elm et al.[64] Finally, the original, unscaled ωB97X-D frequencies were adjusted by a factor of 0.95 to ensure a clear and accurate comparison with the experimental spectra.[65]

RESULTS

Mass Spectrometry and Collision-Induced Dissociation. The clusters discussed in this work will be referred to using the following nomenclature: $(C_2H_5NO_2)_x(NH_3)_y(H_2SO_4)_zH^+ = (G)_x(A)_y(SA)_z$. Figure 1 shows mass spectra obtained by electrospraying two solutions with different ratios of G to ammonium sulfate (1:1, top; 1:3, bottom trace). Equal concentrations of G and ammonium sulfate result in an irregular pattern of clusters only at low m/z. Tripling the concentration of ammonium sulfate, however, results in a drastically different mass spectrum, wherein clusters are observed over a much larger m/z range in addition to a now apparent distribution pattern. A closer inspection of the peaks observed in the bottom trace reveals that the observed pattern corresponds to the formation of three types of clusters: ammonium bisulfate clusters, glycine bisulfate clusters, and mixed clusters with varying numbers of G, A, and SA. The inset in Figure 1 is an example of all three cluster types, separated by 1 m/z. Ammonium bisulfate clusters are well-studied,[5,16,18,24,26,27,66] and here we have focused on some example clusters of the latter two types. A majority of the G-containing clusters are singly charged. The number of SA molecules in each cluster is consistently one less than the sum of G and A per cluster, mirroring ammonium bisulfate clusters with the empirical formula $(G)_0(A)_y(SA)_z$ (where $y = z + 1$). This similarity suggests that G behaves as a base. As shown in Figures S1 and S2, under similar conditions, we only observed anionic clusters over a small m/z range that were predominantly composed of SA and bisulfate only. Figures S3 and S4 display the clusters observed in the bottom trace of Figure 1 in terms of the total number of G and SA per cluster.

In order to gain insight into the strength of the intermolecular interactions stabilizing the clusters, we carried out CID experiments. Figure 2 shows NCE-resolved breakdown curves for the $(G)_0(A)_3(SA)_2$, $(G)_1(A)_2(SA)_2$, $(G)_2(A)_1(SA)_2$, and $(G)_3(A)_0(SA)_2$ clusters, and Figures S5−S8 show the corresponding NCE resolved mass spectra. The major fragments from the pure ammonium bisulfate cluster as well as the mixed clusters with G and A are those

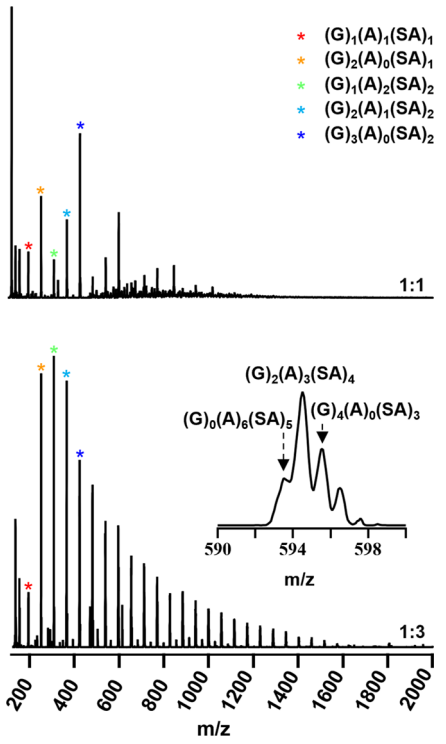

Figure 1. Mass spectrum of (Top) 1 mM glycine/1 mM ammonium sulfate and (Bottom) 1 mM glycine/3 mM ammonium sulfate in 75%/25% acetonitrile/water with 0.1% formic acid. The cationic clusters discussed in this work alone are marked by colored *. The inset image depicts a zoomed-in region of the spectrum illustrating all three cluster compositions.

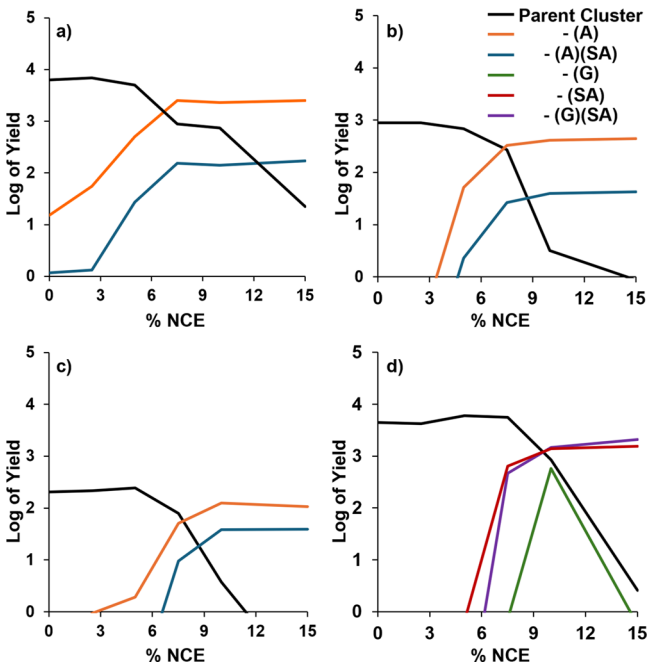

Figure 2. NCE-resolved breakdown curves of (a) $(G)_0(A)_3(SA)_2$, (b) $(G)_1(A)_2(SA)_2$, (c) $(G)_2(A)_1(SA)_2$, and (d) $(G)_3(A)_0(SA)_2$. Each trace is colored to depict a specific fragmentation pathway.

https://doi.org/10.1021/acs.jpca.4c01629
J. Phys. Chem. A 2024, 128, 4268−4278

resulting from the loss of neutral A and the loss of (A)(SA). The loss of A and (A)(SA) is chemically intuitive in the case of the $(G)_0(A)_3(SA)_2$. This result is consistent with earlier work on thermal, surface-induced, and multiphoton-induced dissociation of ammonium bisulfate clusters.[18,67,68] Both mixed clusters exhibit the exact same fragmentation pathways, indicating that it is energetically favorable to retain G in comparison to A or (A)(SA). Fragments arising from the loss of G and SA from these clusters remain undetected. The major fragmentation pathways for a glycine bisulfate cluster $(G)_3(A)_0(SA)_2$ are the loss of neutral G, the loss of SA, and the loss of (G)(SA). As shown in Figures 2 and S8, these three fragmentation pathways begin at higher collisional energies than those required for A and (A)(SA) loss (from the mixed clusters), indicating that more energy is required to remove G or (G)(SA) from the cluster. It is notable that $(G)_3(A)_0(SA)_2$ readily loses (G)(SA) rather than G. The undetected G-loss fragment from the mixed clusters, as well as the ready loss of A, led us to hypothesize that G is more strongly bound to sulfuric acid than ammonia in the mixed clusters.

Considering the 30 ms activation time applied for the CID experiments, we aimed to validate that A and (A)(SA) loss are the predominant fragmentation pathways for the mixed clusters through multiphoton-induced dissociation experiments in our custom-built instrument. While we observed a small fragment yield resulting from the loss of SA in addition to the loss of A and (A)(SA) from the $(G)_1(A)_2(SA)_2$ cluster, once again, we detected no fragments from the dissociation of G in either mixed cluster. Tables S1 and S2 list the yield of each fragment detected when adjusted for microchannel plate detection efficiencies at an operating voltage of 2.3 kV. Furthermore, while keeping the reflectron voltage constant, we observed that although the yield of the A and (A)(SA) loss fragments increased with laser power (as shown in Figures S9 and S10), we detected no fragments arising from the loss of other cluster components from either cluster.

The computed free energies for removing various neutral and ionic components from the $(G)_1(A)_2(SA)_2$ cluster are summarized in Table 1, with details of the calculations provided in the SI. Note that the free energies listed in Table 1 were computed for three different scenarios. Given the 30 ms activation time of the CID experiments, it is likely that the remaining cluster underwent geometry reoptimization. The "Optimized" free energies required for removing a single neutral A, G, or SA from the $(G)_1(A)_2(SA)_2$ are close enough (~2 kcal mol^{-1}) to suggest a potential competition between A, G, and SA to remain in the cluster. This contradicts the CID experiment, where we observed no fragment corresponding to the loss of G or SA. Additionally, the energy required to remove (A)(SA) from this cluster is substantially higher (>10 kcal mol^{-1}) than the energy required to remove G or SA. Yet, our CID results show that the loss of (A)(SA) is a major fragmentation pathway for this cluster. A plausible explanation for these differences could be that the experimentally and computationally probed clusters feature different structures, prompting us to study the structures of the five selected clusters through gas-phase vibrational spectroscopy.

Table 1. Free Energies (in kcal mol^{-1}) for Removing Specific Components from $(G)_1(A)_2(SA)_2$ at 298 K[a]

component (s) removed	frozen	optimized	global minimum
NH_3	43.13	18.18	17.00
NH_4^+	54.65	41.55	
H_2SO_4	41.47	20.93	
HSO_4^-	190.49	166.64	
$C_2H_5NO_2$	43.93	20.50	20.17
$(NH_3)(H_2SO_4)$	40.93	30.95	29.74
$(NH_4^+)(H_2\ SO_4)$	65.85	58.04	
$(NH_3)_2$	69.48	43.39	

[a]"Frozen" and "Optimized" indicate whether the remaining cluster underwent re-optimization of geometry, while "Global Minimum" refers to allowing the remaining cluster to re-optimize to the global minimum.

Results from Vibrational Spectroscopy. We sought to use vibrational spectroscopy to validate our lowest energy computed structures. Examination of these structures revealed numerous configurations existing within 1 kcal mol^{-1} of the apparent global minimum. To that end, we first compare the experimental and calculated spectra for the structures with energies computed at 40 K.

$(G)_1(A)_1(SA)_1$ Cluster. Figure 3 compares the experimental spectrum of $(G)_1(A)_1(SA)_1$ with the spectra of the three lowest energy calculated structures. There are two transitions above 3500 cm^{-1} with comparable intensities. The free bisulfate O−H stretch of ammonium bisulfate clusters has been observed above 3600 cm^{-1}, while matrix isolation and gas

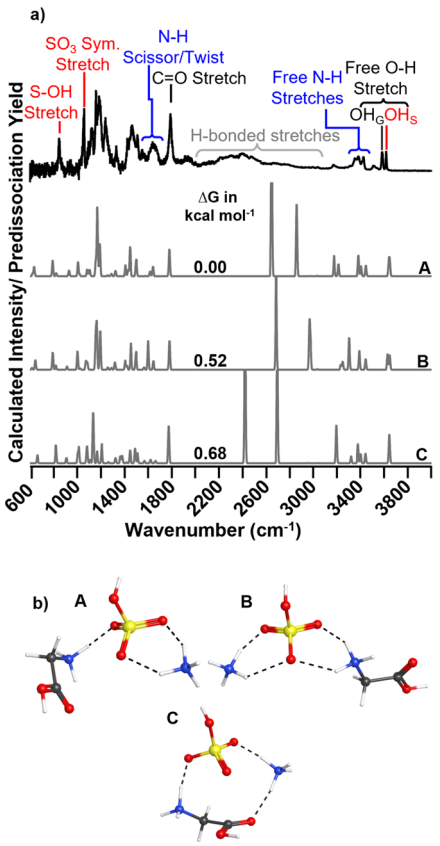

Figure 3. (a) Experimental CIVP spectrum and calculated spectra of the $(G)_1(A)_1(SA)_1$ cluster. The DLPNO−CCSD(T) ΔG value (kcal mol^{-1}), computed at 40 K, is noted for each calculated spectrum. Modes associated with the bisulfate moieties are labeled in red, ammonia modes are in blue, glycine modes are in black, and hydrogen bonded stretches are shown in gray. (b) The structures corresponding to the calculated spectra in (a).

https://doi.org/10.1021/acs.jpca.4c01629
J. Phys. Chem. A 2024, 128, 4268−4278

phase FT−IR spectra of G have reported the carboxylic free O−H stretch between 3570−3590 cm^{-1}.[69,70] We assign the carboxylic acid-free O−H in the $(G)_1(A)_1(SA)_1$ cluster to the transition centered at 3567 cm^{-1} and the bisulfate free O−H to the transition at 3609 cm^{-1} (denoted as "OH_G" and "OH_S" in the spectrum, respectively). The small, low intensity peak at 3505 cm^{-1} has no clear structural origin. In order to identify the spectral manifestations of tag-induced red-shifts, we collected the D_2-tagged CIVP spectrum of this cluster shown in Figure S11. D_2 tagging does not significantly affect the peak at 3505 cm^{-1}, suggesting that the origin of this peak cannot be explained as tag effect alone. However, the peak at 3338 cm^{-1} is an N_2 tag-induced red-shift of the free NH stretch that is not reproduced in the D_2-tagged CIVP spectrum. Lower in energy is a set of three peaks belonging to the stretching motion of the free N−H of both ammonia and glycine. The broad, relatively intense feature between 2000 and 3100 cm^{-1} corresponds to the set of anharmonic features arising from hydrogen-bonded moieties in the cluster.[71−74] Also based on the literature precedent, we assign the dominant modes below 1900 cm^{-1} as the carbonyl C═O stretch at 1785 cm^{-1}, the N−H scissor/twist, and N−H in-phase bending modes at 1633 and 1546 cm^{-1}, the SO_3 asymmetric stretch at 1234 cm^{-1} and symmetric stretch at 1055 cm^{-1}, and finally the S−OH stretch at 842 cm^{-1}.[18,24,27,70,75] The carbonyl C═O stretching transition of glycine has been previously observed at 1790 cm^{-1}, suggesting that the observed small (∼5 cm^{-1}) shift is likely due to a hydrogen bonding interaction between the carbonyl group and a hydrogen bond donor in the cluster.[70,75]

Computed spectra and structures for the lowest energy isomers are shown in Figure 3. Figure S12 shows the vibrational mode assignment for structure A. Structure A is the lowest energy structure, with all three being within the typical uncertainty (1−2 kcal mol^{-1}) associated with quantum chemical calculations of this type.[55] Structures A, B, and C have three, four, and two hydrogen bonds of the NH···OS type, respectively, while Structure C also has an NH···OC hydrogen bond as well.

Inspecting the free O−H stretching region of the calculated spectra, we note that structures A and C feature only one peak, while the experimental spectrum has two. However, on closer inspection, it is clear that the OH_G and OH_S are essentially isoenergetic in structure C but are separated by ∼10 cm^{-1} in structure A. Structure B does reproduce the two free O−H peaks found in the experimental spectrum. However, the complex pattern of peaks in the fingerprint region is not unambiguously reproduced by any calculated spectrum. We hypothesized that the presence of isomers could explain the observed spectral complexity of this region. The IR−IR hole burning spectra shown in Figure S13 make it clear, however, that there is only one isomer experimentally present. The calculated spectra of structures A and B are consistent with the experimental spectrum, although neither spectrum is an exact match.

$(G)_2(A)_0(SA)_1$ Cluster. Figure 4 compares the experimental CIVP spectrum of $(G)_2(A)_0(SA)_1$ with the four lowest energy calculated spectra. The higher energy region of the spectrum once again includes the free OH_S, free OH_G, and the free N−H_2 antisymmetric and symmetric stretches of G. D_2-tagging (shown in Figure S14) establishes that the small peak at 3480 cm^{-1} in Figure 4 is due to the N_2 tag's effect on the free OH_G stretch and the peak at 3346 cm^{-1} is due to the N_2 tag's effect on the free NH stretch. The carbonyl C═O stretch region

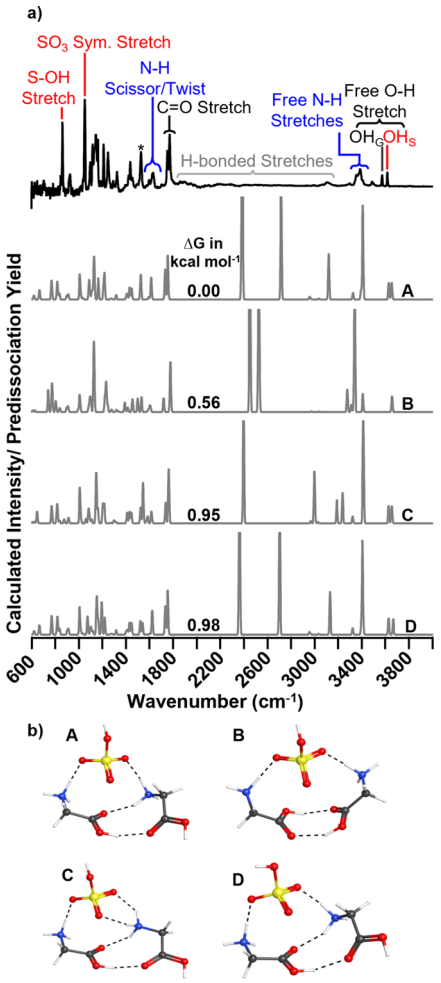

Figure 4. (a) Experimental CIVP spectrum and calculated spectra of the $(G)_2(A)_0(SA)_1$ cluster. The DLPNO−CCSD(T) ΔG value (kcal mol^{-1}), computed at 40 K, is noted for each calculated spectrum. Modes associated with the bisulfate moieties are labeled in red, ammonia modes are in blue, glycine modes are in black, and hydrogen bonded stretches are shown in gray. The NH_3 in-phase bend is marked by *. (b) Structures corresponding to the calculated spectra in (a).

appears as doublet at 1746 and 1766 cm^{-1}, suggesting that the two carbonyls are likely in slightly different hydrogen bonding environments. In the fingerprint region, we observe distinct bisulfate modes, including the S−OH stretch and SO_3 stretches. However, deducing the origin of the other peaks in this region proves to be challenging. Therefore, we turn to inspect the calculated spectra and structures.

Figure 4 also contains the computed spectra and structures of the four isomers within 1 kcal mol^{-1}. Figure S15 shows the vibrational mode assignment for structure A. All but structure B exhibit two free O−H peaks that correspond to a free OH_G and OH_S, as found experimentally. Thus, we initially focus on A, C, and D to identify the experimentally present structure. All three structures reproduce the splitting of the carbonyl stretching feature. Next, the sharp peak corresponding to the NH_3 in-phase bend (marked by *) is well reproduced only in the spectrum of structure A. In structures C and D, this mode appears to be split, owing to the amino group of one G being involved in multiple hydrogen bonds, thereby arresting this bending motion. Additionally, we confirmed that there is only

https://doi.org/10.1021/acs.jpca.4c01629
J. Phys. Chem. A 2024, 128, 4268−4278

one experimentally present isomer via IR−IR hole-burning experiments (as shown in Figure S14). These arguments support structure A being the experimentally probed structure.

$(G)_1(A)_2(SA)_2$ Cluster. Figure 5 shows the CIVP spectrum of this cluster along with the lowest energy calculated spectra.

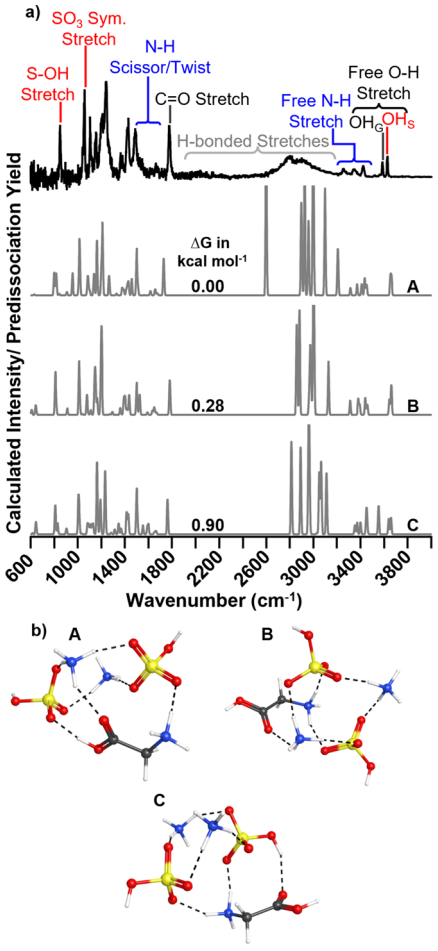

Figure 5. (a) Experimental CIVP spectrum and calculated spectra of the $(G)_1(A)_2(SA)_2$ cluster. The DLPNO−CCSD(T) ΔG value (kcal mol^{-1}), computed at 40 K, is noted for each calculated spectrum. Modes associated with the bisulfate moieties are in red, ammonia modes are in blue, glycine modes are in black, and hydrogen bonded stretches are shown in gray. (b) Structures corresponding to the calculated spectra in (a).

The experimental spectrum is broadly similar to the first two. Of the two peaks in the free O−H stretching region, the OH_S mode (at 3620 cm^{-1}) is more intense than the OH_G, perhaps due to there being more SA than G in this cluster. Two low-intensity peaks at 3500 and 3548 cm^{-1} were revealed to originate from tag-induced effects (see Figure S16). The carbonyl stretching mode is seen at 1773 cm^{-1}. The other distinct modes in the fingerprint region are the S−OH and SO_3 symmetric stretches.

Of the three isomers shown in Figure 5, A and B are essentially isoenergetic, while C is slightly higher in energy. IR−IR hole-burning experiments (shown in Figure S16) established that only one isomer contributes to the experimental spectrum. In structure A, the OH_G is involved in hydrogen bonding, and the spectrum features a single peak above 3500 cm^{-1} corresponding to OH_S stretches. Thus, structures B and C are more consistent with the experimentally present structure. The relative intensity patterns of the free O−H and free N−H stretching regions are well reproduced in structure B's spectrum. Additionally, the bisulfate-specific modes in the fingerprint region are best reproduced in structure B's CIVP spectrum, thereby corroborating that B is most likely the experimentally present structure.

$(G)_2(A)_1(SA)_2$ Cluster. The spectrum of the $(G)_2(A)_1(SA)_2$ cluster is shown in Figure 6. The higher energy region of the

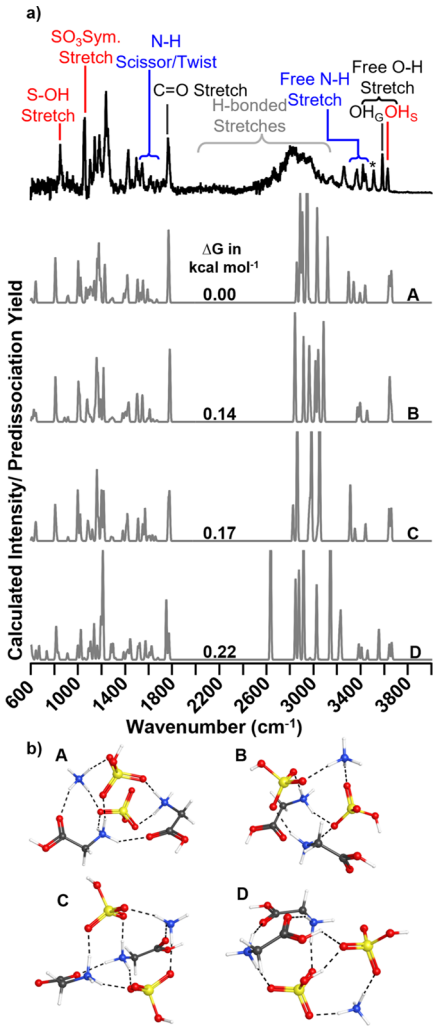

Figure 6. (a) Experimental CIVP spectrum and calculated spectra of the $(G)_2(A)_1(SA)_2$ cluster. The DLPNO−CCSD(T) ΔG value (kcal mol^{-1}), computed at 40 K, is noted for each calculated spectrum. Modes associated with the bisulfate moieties are in red, ammonia modes are in blue, glycine modes are in black, and hydrogen bonded stretches are shown in gray. The new feature at 3505 cm^{-1} is marked by *. (b) Structures corresponding to the calculated spectra in (a).

spectrum features a new intense peak at 3505 cm^{-1} (marked by *) that was not observed in the previously discussed spectra. This peak remains unaffected by D_2 tagging, as illustrated in Figure S19, showing only a slight broadening attributed to saturation effects. This observation establishes that the peak is not influenced significantly by strong tag effects, thereby suggesting that it likely highlights a new hydrogen bonding arrangement in the cluster. The carbonyl stretch appears at 1761 cm^{-1}. This cluster has an equal number of G and SA, but the experimental spectrum shows that the OH_S peak has a

https://doi.org/10.1021/acs.jpca.4c01629
J. Phys. Chem. A 2024, 128, 4268−4278

substantially lower intensity. While the intensities of IR peaks are not additive, this detail serves as evidence in support of a new bonding motif involving the bisulfate moieties of the cluster. The experimental spectrum does not provide any more direct structural insights.

The four lowest-energy isomers are depicted in Figure 6. Structure D's spectrum reproduces the new peak above 3500 cm^{-1}. Only structure D features a unique bonding arrangement in which one bisulfate S═O group accepts two hydrogen bonds: one from the second bisulfate O−H, and another from the carboxylic O−H of a G. The hydrogen bond between the two bisulfate groups is the shortest hydrogen bond in the structure, with a bond length of 1.66 Å. The sharp, intense transition at ∼3600 cm^{-1} in the calculated spectrum corresponds to the coupled stretching motion of this unique three-way interaction. However, the complex pattern in this region also raises the possibility of contributions from more than one isomer. We obtained the spectrum (NH and OH stretching regions) of the second isomer (magenta trace shown in Figure S19) using hole burning to remove the population of the isomer that absorbs at 3505 cm^{-1}. The peaks between 3400 and 3452 cm^{-1} in the experimental spectrum originate from the two different isomers, respectively. Boltzmann population analysis, as described in the Supporting Information, was conducted at both D_2- and N_2-tagging temperatures (47 and 17 K, respectively, as shown in Figure S20). Neglecting the contribution of the tag, the analysis revealed that the two isomers are close in energy, with a difference of approximately 0.03−0.06 kcal mol^{-1}.

Of the nine low-lying structures (shown in Figure S21) computed for this cluster, six structures have the bisulfate moieties involved in a hydrogen bonding arrangement with each other. Bisulfate−bisulfate hydrogen bonding was found to be important to the structure of the dry $(G)_0(A)_4(SA)_3$ and larger ammonium bisulfate clusters.[27] While the $(G)_2(A)_1(SA)_2$ is smaller than the $(G)_0(A)_4(SA)_3$ in terms of total number of cluster components, we hypothesize that the presence of the bulkier G encourages the formation of the bisulfate-bisulfate hydrogen bond. Kreinbihl and co-workers were able to identify and assign the out-of-plane OH bending transition characteristic of this type of hydrogen bonding.[27] However, the region between 1300−1400 cm^{-1} is rather complex here and prevents us from explicitly identifying the same spectral signature.

$(G)_3(A)_0(SA)_2$ Cluster. The experimental spectrum of the $(G)_3(A)_0(SA)_2$ cluster along with the lowest energy calculated spectra are shown in the Figure 7. A direct comparison to the $(G)_2(A)_0(SA)_1$ spectrum allows us to obtain some qualitative information on the structure. In the experimental spectrum, the carbonyl stretching mode is partially resolved into peaks centered at 1781 and 1768 cm^{-1}, with a small shoulder at 1739 cm^{-1}. The observed splitting is characteristic of all three carbonyls being involved in hydrogen bonding, with the degree of splitting a direct indication of the local hydrogen bonding environments of each carbonyl group.[70,76,77] Below 1730 cm^{-1}, the S−OH stretch and the SO_3 symmetric stretch are the most notable features in the spectrum. All other transitions are rather diffuse and limit our ability to extract structural information solely from the experimental spectrum.

A quick appraisal of the low-energy candidate structures establishes the presence of the bisulfate−bisulfate hydrogen bond in all four structures. Structures A, B, and D reproduce the relative intensity pattern of the carbonyl stretching mode.

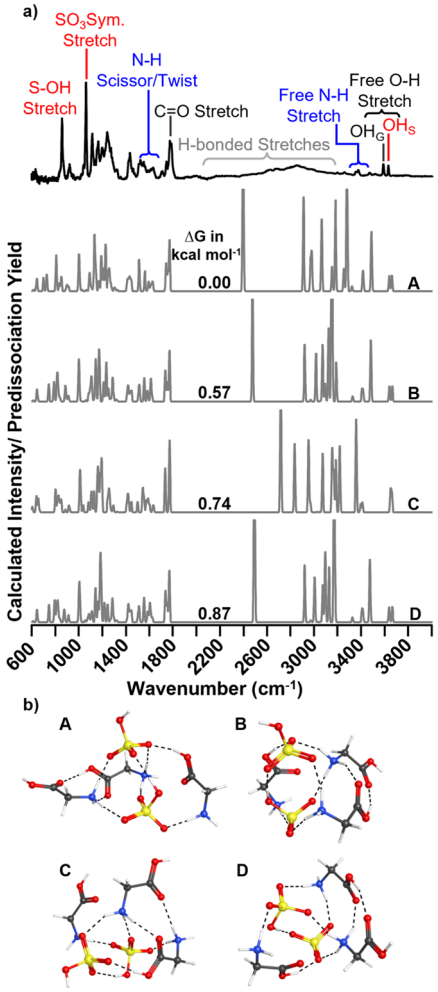

Figure 7. (a) Experimental CIVP spectrum (top) and calculated spectra (bottom) of the $(G)_3(A)_0(SA)_2$ cluster. The DLPNO−CCSD(T) ΔG value in (kcal mol^{-1}), computed at 40 K, is mentioned on each calculated spectrum. Modes associated with the bisulfate moieties are in red, ammonia modes are in blue, glycine modes are in black, and hydrogen bonded stretches are shown in gray. (b) Structures corresponding to the calculated spectra in (a).

Of these, we find that the relative intensities of the bisulfate-specific modes below 1000 cm^{-1} are well reproduced in structure A's spectrum while the spectra of B and D display more complexity in this region. IR−IR hole-burning experiments (shown in Figure S23) clarify that only one isomer is present under the experimental conditions. Thus, the similarity between the experimental spectrum and the calculated spectrum suggests that structure A is the experimentally probed structure of the $(G)_3(A)_0(SA)_2$ cluster.

DISCUSSION

Temperature−Structure Relationship. Figures S24−S28 along with Tables S4−S8 compare the low energy structures of all five clusters across three different temperatures. For clusters $(G)_1(A)_1(SA)_1$ and $(G)_1(A)_2(SA)_2$, structures A and B change order at warmer temperatures. While this raises the possibility that structure B of the $(G)_1(A)_2(SA)_2$ cluster was the structure probed by both the CID and IRMPD experiments (since both experiments were carried out at room temperature) and CIVP experiment, the energy differences between structures A and B at warmer

https://doi.org/10.1021/acs.jpca.4c01629
J. Phys. Chem. A 2024, 128, 4268−4278

temperatures also heighten the likelihood of both structures coexisting. In the case of the $(G)_2(A)_0(SA)_1$ and the $(G)_2(A)_1(SA)_2$ clusters, structure A remains the calculated minimum energy structure while a significant number of the other structures computed for these two clusters fall within 1 kcal mol^{-1} at higher temperatures. As for $(G)_3(A)_0(SA)_2$, structure E is the minimum at 217 and 298 K and structure A is only slightly higher in energy. Put together, it is evident that temperature plays a significant role in determining the minimum energy structure as well as the energetic ordering of close-lying isomers of the five clusters studied in this work. Cluster growth models that are currently employed assume that only one isomer (the minimum energy structure) is likely to contribute to growth.[78] However, if the energy differences between isomers are low enough, more than one isomer can exist as well as contribute to particle growth at atmospherically relevant temperatures. Thus, it is imperative to re-evaluate the role played by isomers, especially for molecules with many potential conformations, in particle growth under atmospheric conditions.

Glycine Competes with Ammonia to Stabilize Sulfuric Acid. The impact of base stabilization on sulfate aerosol formation is well established, with synergistic effects between a mixture of different bases promoting nucleation to a greater extent than a single base. For example, amines encourage proton transfer reactions and have a larger stabilization effect on smaller clusters while ammonia's smaller size makes it the ideal candidate for encouraging growth by maximizing the total number of hydrogen bonds between cluster constituents.[17] Based on pK_a and gas phase proton affinity, glycine is a slightly stronger base than ammonia while also simultaneously being capable of forming more intermolecular interactions than amines such as methylamine and dimethylamine. Under the premise of the principle of microscopic reversibility, fragmentation pathways are the reverse of the formation pathways. Irrespective of whether the mixed clusters were activated on a millisecond time scale (CID) or by a few nanosecond long infrared pulse (IRMPD), the dissociation pathways were always the loss of ammonia or the loss of ammonia and sulfuric acid. This implies that glycine is more strongly bound within the cluster. While the atmospheric abundance of free glycine is currently unknown, it is, however, apparent that if present together, glycine will compete with ammonia to bind to sulfuric acid. Given that a small concentration of glycine (compared to ammonia and sulfuric acid) is adequate to facilitate extensive cluster formation among the three components, it is plausible to consider that a replacement of ammonia by glycine might be a part of the aging process of new particles.

Potential Incipient Phase Separation. Bisulfate−bisulfate hydrogen bonds that are prevalent in the $(G)_2(A)_1(SA)_2$ and $(G)_3(A)_0(SA)_2$ clusters are retained in structures calculated at lower-tropospheric temperatures (Figures S27−S31), suggesting that this binding motif will probably play a role in the growth of such clusters. Sulfuric acid prefers to bind to sulfuric acid, ammonia, or the amino end of glycine while glycine prefers to bind to glycine or ammonia. This implies a preference for organic components to bond with one another and for inorganic components within the clusters to preferentially bind to other inorganic components. Such an arrangement can influence the selectivity of these clusters in accommodating incoming molecules during nucleation. To elaborate, an incoming inorganic species such as sulfuric acid is likely to bind to the free N−H groups and bisulfate O−H on the surface of such clusters, while an organic species such as dicarboxylic acid is likely to preferentially add to the side with free carboxylic O−H groups. Such selectivity would presumably affect which functional groups are likely to be present on the surface of the cluster, thereby influencing aerosol growth, aging, and hygroscopic properties.

SUMMARY

We investigated the composition, stability, and structures of clusters of G, A, and SA using mass spectrometry, vibrational spectroscopy, and quantum chemical calculations. Our calculations suggest that the energies required to remove G, A, or SA from a mixed cluster $(G)_1(A)_2(SA)_2$ are comparable. Collision-induced and multiphoton-induced dissociation experiments have established that the preferred loss pathway involves the neutral A, with G loss never observed unless the cluster lacks any A to lose. This observation suggests that G likely exerts a larger stabilizing effect on SA. Identifying the experimentally present structure was challenging due to the complexity of the spectra and the likely influence of anharmonic effects. Calculations suggest the presence of bisulfate−bisulfate hydrogen bonds in $(G)_2(A)_1(SA)_2$ and $(G)_3(A)_0(SA)_2$ clusters. Only a few structures exhibit direct interactions between carboxylic O−H and bisulfate S═O, indicating possible phase separation between the organic and inorganic constituents even at these small sizes. While only a few demonstrative clusters were sampled, our work provides experimental evidence that G could play a complex role in clusters of this type if present in the atmosphere. It would likely efficiently displace ammonia in new particles. Furthermore, these clusters have many close-lying isomers at relevant temperatures, highlighting potentially important entropic effects in models of particle growth at atmospherically relevant temperatures.

ASSOCIATED CONTENT

Supporting Information

The Supporting Information is available free of charge at https://pubs.acs.org/doi/10.1021/acs.jpca.4c01629.

Methods used to compute the binding free energies for all clusters as well as the Boltzmann population analysis used for $(G)_2(A)_1(SA)_2$, collisional energy-resolved CID mass spectra for all five clusters, comparison of the experimental vibrational spectrum to all candidate structures under 2 kcal/mol for all clusters, experimental isomer-selective spectra for all five clusters, comparison of tag effects on the spectrum of $(G)_1(A)_1(SA)_1$, $(G)_2(A)_0(SA)_1$, $(G)_1(A)_2(SA)_2$, and $(G)_2(A)_1(SA)_2$ clusters, calculated atomic coordinates for all clusters, tabulated infrared multiphoton dissociation yields for the $(G)_1(A)_2(SA)_2$ and $(G)_2(A)_1(SA)_2$, energetic ordering of structures calculated at different temperatures for all five clusters, and the Boltzmann population of isomers of the $(G)_2(A)_1(SA)_2$ cluster (PDF)

AUTHOR INFORMATION

Corresponding Author

Christopher J. Johnson − *Department of Chemistry, Stony Brook University, Stony Brook, New York 11794, United States;* orcid.org/0000-0003-1859-5615; Email: chris.johnson@stonybrook.edu

https://doi.org/10.1021/acs.jpca.4c01629
J. Phys. Chem. A 2024, 128, 4268−4278

Authors

Annapoorani Hariharan − *Department of Chemistry, Stony Brook University, Stony Brook, New York 11794, United States;* orcid.org/0000-0002-9995-2700

Conor J. Bready − *Department of Chemistry, Furman University, Greenville, South Carolina 29613, United States;* orcid.org/0000-0001-5879-7786

Jack G. Ajello − *Department of Chemistry, Stony Brook University, Stony Brook, New York 11794, United States*

Samantha H. Black − *Department of Chemistry, Stony Brook University, Stony Brook, New York 11794, United States*

George C. Shields − *Department of Chemistry, Furman University, Greenville, South Carolina 29613, United States;* orcid.org/0000-0003-1287-8585

Complete contact information is available at: https://pubs.acs.org/10.1021/acs.jpca.4c01629

Notes

The authors declare no competing financial interest.

■ ACKNOWLEDGMENTS

S.H.B. acknowledges support from the National Science Foundation Research Experience for Undergraduates (grant no. CHE-2050541). A.H. and C.J.J. gratefully acknowledge the National Science Foundation for supporting this work under grant CHE-1905172. C.J.B. acknowledges support from the Barry M. Goldwater Scholarship. G.C.S. acknowledges the National Science Foundation for supporting this work under grants CHE-2320718 and CHE-2018427. Any opinions, findings, conclusions, or recommendations expressed in this material are those of the author(s) and do not necessarily reflect the views of the National Science Foundation.

■ REFERENCES

(1) Kulmala, M.; et al. Toward direct measurement of atmospheric nucleation. *Science* **2007**, *318*, 89−92.

(2) Kulmala, M.; Kontkanen, J.; Junninen, H.; Lehtipalo, K.; Manninen, H. E.; Nieminen, T.; Petäjä, T.; Sipilä, M.; Schobesberger, S.; Rantala, P.; et al. Direct observations of atmospheric aerosol nucleation. *Science* **2013**, *339*, 943−946.

(3) Kulmala, M. How particles nucleate and grow. *Science* **2003**, *302*, 1000−1001.

(4) Zhang, R. Getting to the critical nucleus of aerosol formation. *Science* **2010**, *328*, 1366−1367.

(5) Bzdek, B. R.; Johnston, M. V. New particle formation and growth in the troposphere. *Anal. Chem.* **2010**, *82*, 7871−7878.

(6) Krejci, R.; Ström, J.; De Reus, M.; Sahle, W. Single particle analysis of the accumulation mode aerosol over the northeast Amazonian tropical rain forest, Surinam South America. *Atmospheric Chemistry and Physics* **2005**, *5*, 3331−3344.

(7) Spracklen, D.; Carslaw, K.; Kulmala, M.; Kerminen, V.-M.; Mann, G.; Sihto, S.-L. The contribution of boundary layer nucleation events to total particle concentrations on regional and global scales. *Atmospheric Chemistry and Physics* **2006**, *6*, 5631−5648.

(8) Merikanto, J.; Spracklen, D.; Mann, G.; Pickering, S.; Carslaw, K. Impact of nucleation on global CCN. *Atmospheric Chemistry and Physics* **2009**, *9*, 8601−8616.

(9) Yu, F.; Luo, G. Simulation of particle size distribution with a global aerosol model: contribution of nucleation to aerosol and CCN number concentrations. *Atmospheric Chemistry and Physics* **2009**, *9*, 7691−7710.

(10) Gordon, H.; Kirkby, J.; Baltensperger, U.; Bianchi, F.; Breitenlechner, M.; Curtius, J.; Dias, A.; Dommen, J.; Donahue, N. M.; Dunne, E. M.; et al. Causes and importance of new particle formation in the present-day and preindustrial atmospheres. *J. Geophys. Res.: Atmos.* **2017**, *122*, 8739−8760.

(11) Hallquist, M.; et al. The formation, properties and impact of secondary organic aerosol: current and emerging issues. *Atmospheric Chemistry and Physics* **2009**, *9*, 5155−5236.

(12) Zhang, R.; Khalizov, A.; Wang, L.; Hu, M.; Xu, W. Nucleation and growth of nanoparticles in the atmosphere. *Chem. Rev.* **2012**, *112*, 1957−2011.

(13) Stocker, T.; Dahe, Q.; Plattner, K. G; Tignor, M.; Allen, K. S; Boschung, J.; Nauels, A.; Xia, Y.; Bex, V.; Midgleym, P. M. *IPCC, 2013: Climate Change 2013: The Physical Science Basis. Working Group I Contribution to the Fifth Assessment Report of the Intergovernmental Panel on Climate Change*; Cambridge University Press: U.K and New York, 2013; p 1535.

(14) Kurtén, T.; Torpo, L.; Ding, C.-G.; Vehkamäki, H.; Sundberg, M. R.; Laasonen, K.; Kulmala, M. A density functional study on water-sulfuric acid-ammonia clusters and implications for atmospheric cluster formation. *J. Geophys. Res.: Atmos.* **2007**, *112*, D04210.

(15) Kurten, T.; Loukonen, V.; Vehkamäki, H.; Kulmala, M. Amines are likely to enhance neutral and ion-induced sulfuric acid-water nucleation in the atmosphere more effectively than ammonia. *Atmospheric Chemistry and Physics* **2008**, *8*, 4095−4103.

(16) DePalma, J. W.; Bzdek, B. R.; Doren, D. J.; Johnston, M. V. Structure and energetics of nanometer size clusters of sulfuric acid with ammonia and dimethylamine. *J. Phys. Chem. A* **2012**, *116*, 1030−1040.

(17) Temelso, B.; Morrison, E. F.; Speer, D. L.; Cao, B. C.; Appiah-Padi, N.; Kim, G.; Shields, G. C. Effect of mixing ammonia and alkylamines on sulfate aerosol formation. *J. Phys. Chem. A* **2018**, *122*, 1612−1622.

(18) Johnson, C. J.; Johnson, M. A. Vibrational spectra and fragmentation pathways of size-selected, D_2-tagged ammonium/methylammonium bisulfate clusters. *J. Phys. Chem. A* **2013**, *117*, 13265−13274.

(19) Almeida, J.; Schobesberger, S.; Kürten, A.; Ortega, I. K.; Kupiainen-Määttä, O.; Praplan, A. P.; Adamov, A.; Amorim, A.; Bianchi, F.; Breitenlechner, M.; et al. Molecular understanding of sulphuric acid−amine particle nucleation in the atmosphere. *Nature* **2013**, *502*, 359−363.

(20) Schobesberger, S.; et al. On the composition of ammonia−sulfuric-acid ion clusters during aerosol particle formation. *Atmospheric Chemistry and Physics* **2015**, *15*, 55−78.

(21) Bianchi, F.; Tröstl, J.; Junninen, H.; Frege, C.; Henne, S.; Hoyle, C. R.; Molteni, U.; Herrmann, E.; Adamov, A.; Bukowiecki, N.; et al. New particle formation in the free troposphere: A question of chemistry and timing. *Science* **2016**, *352*, 1109−1112.

(22) Jen, C. N.; Bachman, R.; Zhao, J.; McMurry, P. H.; Hanson, D. R. Diamine-sulfuric acid reactions are a potent source of new particle formation. *Geophys. Res. Lett.* **2016**, *43*, 867−873.

(23) Elm, J.; Passananti, M.; Kurten, T.; Vehkamaki, H. Diamines can initiate new particle formation in the atmosphere. *J. Phys. Chem. A* **2017**, *121*, 6155−6164.

(24) Waller, S. E.; Yang, Y.; Castracane, E.; Racow, E. E.; Kreinbihl, J. J.; Nickson, K. A.; Johnson, C. J. The interplay between hydrogen bonding and coulombic forces in determining the structure of sulfuric acid-amine alusters. *J. Phys. Chem. Lett.* **2018**, *9*, 1216−1222.

(25) Myllys, N.; Chee, S.; Olenius, T.; Lawler, M.; Smith, J. Molecular-level understanding of synergistic effects in sulfuric acid−amine−ammonia mixed clusters. *J. Phys. Chem. A* **2019**, *123*, 2420−2425.

(26) Waller, S. E.; Yang, Y.; Castracane, E.; Kreinbihl, J. J.; Nickson, K. A.; Johnson, C. J. Electrospray ionization−based synthesis and validation of amine-sulfuric acid clusters of relevance to atmospheric new particle formation. *J. Am. Soc. Mass Spectrom.* **2019**, *30*, 2267−2277.

(27) Kreinbihl, J. J.; Frederiks, N. C.; Waller, S. E.; Yang, Y.; Johnson, C. J. Establishing the structural motifs present in small ammonium and aminium bisulfate clusters of relevance to

atmospheric new particle formation. *J. Chem. Phys.* **2020**, *153*, No. 034307.
(28) Zhang, R.; Suh, I.; Zhao, J.; Zhang, D.; Fortner, E. C.; Tie, X.; Molina, L. T.; Molina, M. J. Atmospheric new particle formation enhanced by organic acids. *Science* **2004**, *304*, 1487−1490.
(29) Metzger, A.; Verheggen, B.; Dommen, J.; Duplissy, J.; Prevot, A. S. H.; Weingartner, E.; Riipinen, I.; Kulmala, M.; Spracklen, D. V.; Carslaw, K. S.; Baltensperger, U. Evidence for the role of organics in aerosol particle formation under atmospheric conditions. *Proc. Natl. Acad. Sci. U. S. A.* **2010**, *107*, 6646−6651.
(30) Tröstl, J.; Chuang, W. K.; Gordon, H.; Heinritzi, M.; Yan, C.; Molteni, U.; Ahlm, L.; Frege, C.; Bianchi, F.; Wagner, R.; et al. The role of low-volatility organic compounds in initial particle growth in the atmosphere. *Nature* **2016**, *533*, 527−531.
(31) Hou, G.-L.; Lin, W.; Wang, X.-B. Direct observation of hierarchic molecular interactions critical to biogenic aerosol formation. *Commun. Chem.* **2018**, *1*, 37.
(32) Wang, C.-Y.; Ma, Y.; Chen, J.; Jiang, S.; Liu, Y.-R.; Wen, H.; Feng, Y.-J.; Hong, Y.; Huang, T.; Huang, W. Bidirectional interaction of alanine with sulfuric acid in the presence of water and the atmospheric implication. *J. Phys. Chem. A* **2016**, *120*, 2357−2371.
(33) Elm, J.; Myllys, N.; Kurten, T. What is required for highly oxidized molecules to form clusters with sulfuric acid? *J. Phys. Chem. A* **2017**, *121*, 4578−4587.
(34) Zhang, Q.; Anastasio, C.; Jimenez-Cruz, M. Water-soluble organic nitrogen in atmospheric fine particles (PM2.5) from Northern California. *J. Geophys. Res.: Atmos.* **2002**, *107*, AAC 3-1−AAC 3-9.
(35) Zhang, Q.; Anastasio, C. Free and combined amino compounds in atmospheric fine particles (PM2.5) and fog waters from Northern California. *Atmos. Environ.* **2003**, *37*, 2247−2258.
(36) Mader, B.; Yu, J.; Xu, J.; Li, Q.; Wu, W. S.; Flagan, R. C.; Seinfeld, J. H. Molecular composition of the water-soluble fraction of atmospheric carbonaceous aerosols collected during ACE-Asia. *J. Geophys. Res.: Atmos.* **2004**, *109*, D06206.
(37) Matos, J. T.; Duarte, R. M.; Duarte, A. C. Challenges in the identification and characterization of free amino acids and proteinaceous compounds in atmospheric aerosols: A critical review. *TrAC, Trends in Analytical Chemistry* **2016**, *75*, 97−107.
(38) Kristensson, A.; Rosenørn, T.; Bilde, M. Cloud droplet activation of amino acid aerosol particles. *J. Phys. Chem. A* **2010**, *114*, 379−386.
(39) Li, X.; Hede, T.; Tu, Y.; Leck, C.; Ågren, H. Cloud droplet activation mechanisms of amino acid aerosol particles: insight from molecular dynamics simulations. *Tellus B: Chemical and Physical Meteorology* **2022**, *65*, 20476.
(40) Mocellin, A.; Gomes, A. H. d. A.; Araújo, O. C.; De Brito, A. N.; Bjorneholm, O. Surface propensity of atmospherically relevant amino acids studied by XPS. *J. Phys. Chem. B* **2017**, *121*, 4220−4225.
(41) Triesch, N.; van Pinxteren, M.; Salter, M.; Stolle, C.; Pereira, R.; Zieger, P.; Herrmann, H. Sea spray aerosol chamber study on selective sransfer and enrichment of free and combined amino acids. *ACS Earth Space Chem.* **2021**, *5*, 1564−1574.
(42) Angle, K. J.; Nowak, C. M.; Davasam, A.; Dommer, A. C.; Wauer, N. A.; Amaro, R. E.; Grassian, V. H. Amino acids are driven to the interface by salts and acidic environments. *J. Phys. Chem. Lett.* **2022**, *13*, 2824−2829.
(43) Mopper, K.; Zika, R. G. Free amino acids in marine rains: evidence for oxidation and potential role in nitrogen cycling. *Nature* **1987**, *325*, 246−249.
(44) Cornell, S.; Mace, K.; Coeppicus, S.; Duce, R.; Huebert, B.; Jickells, T.; Zhuang, L.-Z. Organic nitrogen in Hawaiian rain and aerosol. *J. Geophys. Res.:Atmos.* **2001**, *106*, 7973−7983.
(45) Kuznetsova, M.; Lee, C.; Aller, J.; Frew, N. Enrichment of amino acids in the sea surface microlayer at coastal and open ocean sites in the North Atlantic Ocean. *Limnology and Oceanography* **2004**, *49*, 1605−1619.
(46) Mandalakis, M.; Apostolaki, M.; Tziaras, T.; Polymenakou, P.; Stephanou, E. G. Free and combined amino acids in marine background atmospheric aerosols over the Eastern Mediterranean. *Atmos. Environ.* **2011**, *45*, 1003−1009.
(47) Scalabrin, E.; Zangrando, R.; Barbaro, E.; Kehrwald, N.; Gabrieli, J.; Barbante, C.; Gambaro, A. Amino acids in Arctic aerosols. *Atmospheric Chemistry and Physics* **2012**, *12*, 10453−10463.
(48) Song, T.; Wang, S.; Zhang, Y.; Song, J.; Liu, F.; Fu, P.; Shiraiwa, M.; Xie, Z.; Yue, D.; Zhong, L.; et al. Proteins and amino acids in fine particulate matter in rural Guangzhou, Southern China: Seasonal Cycles, Sources, and Atmospheric Processes. *Environ. Sci. Technol.* **2017**, *51*, 6773−6781.
(49) Helin, A.; Sietiö, O.-M.; Heinonsalo, J.; Bäck, J.; Riekkola, M.-L.; Parshintsev, J. Characterization of free amino acids, bacteria and fungi in size-segregated atmospheric aerosols in boreal forest: seasonal patterns, abundances and size distributions. *Atmospheric Chemistry and Physics* **2017**, *17*, 13089−13101.
(50) Ge, P.; Luo, G.; Luo, Y.; Huang, W.; Xie, H.; Chen, J.; Qu, J. Molecular understanding of the interaction of amino acids with sulfuric acid in the presence of water and the atmospheric implication. *Chemosphere* **2018**, *210*, 215−223.
(51) Ren, L.; Bai, H.; Yu, X.; Wu, F.; Yue, S.; Ren, H.; Li, L.; Lai, S.; Sun, Y.; Wang, Z.; et al. Molecular composition and seasonal variation of amino acids in urban aerosols from Beijing China. *Atmos. Res.* **2018**, *203*, 28−35.
(52) Renard, P.; Brissy, M.; Rossi, F.; Leremboure, M.; Jaber, S.; Baray, J.-L.; Bianco, A.; Delort, A.-M.; Deguillaume, L. Free amino acid quantification in cloud water at the Puy de Dôme station (France). *Atmospheric Chemistry and Physics* **2022**, *22*, 2467−2486.
(53) Ball, B. T.; Vanovac, S.; Odbadrakh, T. T.; Shields, G. C. Monomers of glycine and serine have a limited ability to hydrate in the atmosphere. *J. Phys. Chem. A* **2021**, *125*, 8454−8467.
(54) Elm, J.; Fard, M.; Bilde, M.; Mikkelsen, K. V. Interaction of glycine with common atmospheric nucleation precursors. *J. Phys. Chem. A* **2013**, *117*, 12990−12997.
(55) Bready, C. J.; Vanovac, S.; Odbadrakh, T. T.; Shields, G. C. Amino acids compete with ammonia in sulfuric acid-based atmospheric aerosol prenucleation: the case of glycine and serine. *J. Phys. Chem. A* **2022**, *126*, 5195−5206.
(56) Frederiks, N. C.; Heaney, D. D.; Kreinbihl, J. J.; Johnson, C. J. The competition between hydrogen, halogen, and covalent bonding in atmospherically relevant ammonium iodate clusters. *J. Am. Chem. Soc.* **2023**, *145*, 1165−1175.
(57) Elliott, B. M.; Relph, R. A.; Roscioli, J. R.; Bopp, J. C.; Gardenier, G. H.; Guasco, T. L.; Johnson, M. A. Isolating the spectra of cluster ion isomers using Ar-"tag"-mediated IR-IR double resonance within the vibrational manifolds: Application to $NO_2^-\cdot H_2O$. *J. Chem. Phys.* **2008**, *129*, No. 094303.
(58) Leavitt, C. M.; Wolk, A. B.; Fournier, J. A.; Kamrath, M. Z.; Garand, E.; Van Stipdonk, M. J.; Johnson, M. A. Isomer-specific IR−IR double resonance spectroscopy of D_2-tagged protonated dipeptides prepared in a cryogenic ion trap. *J. Phys. Chem. Lett.* **2012**, *3*, 1099−1105.
(59) Dieterich, J. M.; Hartke, B. OGOLEM: Global cluster structure optimization for arbitrary mixtures of flexible molecules. A multi-scaling, object-oriented approach. *Mol. Phys.* **2010**, *108*, 279−291.
(60) Dieterich, J. M.; Hartke, B. Empirical review of standard benchmark functions using evolutionary global optimization. *Appl. Math.* **2012**, *3*, 1552−1564.
(61) Frisch, M. J.; Trucks, G. W.; Schlegel, H. B.; Scuseria, G. E.; Robb, M. A.; Cheeseman, J. R.; Scalmani, G.; Barone, V.; Petersson, G. A.; Nakatsuji, H. et al. *Gaussian 16 Revision B.01*; Gaussian Inc.: Wallingford CT, 2016.
(62) Odbadrakh, T. T.; Gale, A. G.; Ball, B. T.; Temelso, B.; Shields, G. C. Computation of atmospheric concentrations of molecular clusters from ab initio thermochemistry. *J. Vis. Exp.* **2020**, *158*, No. e60964.
(63) Kurfman, L. A.; Odbadrakh, T. T.; Shields, G. C. Calculating reliable Gibbs free energies for formation of gas-phase clusters that are critical for atmospheric chemistry: $(H_2SO_4)_3$. *J. Phys. Chem. A* **2021**, *125*, 3169−3176.

https://doi.org/10.1021/acs.jpca.4c01629
J. Phys. Chem. A 2024, 128, 4268−4278

(64) Elm, J.; Ayoubi, D.; Engsvang, M.; Jensen, A. B.; Knattrup, Y.; Kubečka, J.; Bready, C. J.; Fowler, V. R.; Harold, S. E.; Longsworth, O. M.; et al. Quantum chemical modeling of organic enhanced atmospheric nucleation: A critical review. *Wiley Interdiscip. Rev.: Comput. Mol. Sci.* **2023**, *13*, No. e1662.
(65) Kanchanakungwankul, S.; Bao, J.; Zheng, J.; Alecu, I.; Lynch, B.; Zhao, Y.; Truhlar, D. *Database of Frequency Scale Factors for Electronic Model Chemistries—Version 5*, 2021.
(66) Bzdek, B. R.; DePalma, J. W.; Johnston, M. V. Mechanisms of atmospherically relevant cluster growth. *Acc. Chem. Res.* **2017**, *50*, 1965−1975.
(67) Froyd, K. D.; Lovejoy, E. R. Bond energies and structures of ammonia−sulfuric acid positive cluster ions. *J. Phys. Chem. A* **2012**, *116*, 5886−5899.
(68) Bzdek, B. R.; DePalma, J. W.; Ridge, D. P.; Laskin, J.; Johnston, M. V. Fragmentation energetics of clusters relevant to atmospheric new particle formation. *J. Am. Chem. Soc.* **2013**, *135*, 3276−3285.
(69) Stepanian, S.; Reva, I.; Radchenko, E.; Rosado, M.; Duarte, M.; Fausto, R.; Adamowicz, L. Matrix-isolation infrared and theoretical studies of the glycine conformers. *J. Phys. Chem. A* **1998**, *102*, 1041−1054.
(70) Linder, R.; Seefeld, K.; Vavra, A.; Kleinermanns, K. Gas phase infrared spectra of nonaromatic amino acids. *Chem. Phys. Lett.* **2008**, *453*, 1−6.
(71) Headrick, J. M.; Diken, E. G.; Walters, R. S.; Hammer, N. I.; Christie, R. A.; Cui, J.; Myshakin, E. M.; Duncan, M. A.; Johnson, M. A.; Jordan, K. D. Spectral signatures of hydrated proton vibrations in water clusters. *Science* **2005**, *308*, 1765−1769.
(72) Roscioli, J.; McCunn, L.; Johnson, M. Quantum structure of the intermolecular proton bond. *Science* **2007**, *316*, 249−254.
(73) Johnson, C. J.; Dzugan, L. C.; Wolk, A. B.; Leavitt, C. M.; Fournier, J. A.; McCoy, A. B.; Johnson, M. A. Microhydration of contact ion pairs in $M^{2+}OH^{-}$-(H_2O) n= 1−5 (M= Mg, Ca) clusters: spectral manifestations of a mobile proton defect in the first hydration shell. *J. Phys. Chem. A* **2014**, *118*, 7590−7597.
(74) Chen, L.; Ma, Z.; Fournier, J. A. Origins of the diffuse shared proton vibrational signatures in proton-coupled electron transfer model dyad complexes. *J. Chem. Phys.* **2022**, *157*, 154308.
(75) Kumar, S.; Rai, A. K.; Singh, V.; Rai, S. Vibrational spectrum of glycine molecule. *Spectrochim. Acta, Part A* **2005**, *61*, 2741−2746.
(76) Fischer, K. C.; Sherman, S. L.; Voss, J. M.; Zhou, J.; Garand, E. Microsolvation structures of protonated glycine and L-alanine. *J. Phys. Chem. A* **2019**, *123*, 3355−3366.
(77) Sherman, S. L.; Fischer, K. C.; Garand, E. Conformational changes induced by methyl side-chains in protonated tripeptides containing glycine and alanine residues. *J. Phys. Chem. A* **2022**, *126*, 4036−4045.
(78) McGrath, M.; Olenius, T.; Ortega, I.; Loukonen, V.; Paasonen, P.; Kurtén, T.; Kulmala, M.; Vehkamäki, H. Atmospheric Cluster Dynamics Code: a flexible method for solution of the birth-death equations. *Atmospheric Chemistry and Physics* **2012**, *12*, 2345−2355.

https://doi.org/10.1021/acs.jpca.4c01629
J. Phys. Chem. A 2024, 128, 4268−4278